IEEE Access
Multidisciplinary | Rapid Review | Open Access Journal

Received March 25, 2019, accepted April 21, 2019, date of publication May 1, 2019, date of current version May 17, 2019.

Digital Object Identifier 10.1109/ACCESS.2019.2913451

Robust Ride Height Control for Active Air Suspension Systems With Multiple Unmodeled Dynamics and Parametric Uncertainties

RONGCHEN ZHAO[1], WEI XIE[2], PAK KIN WONG[1], DAVID CABECINHAS[2,3], AND CARLOS SILVESTRE[2,3,4], (Member, IEEE)

[1]Department of Electromechanical Engineering, Faculty of Science and Technology, University of Macau, Macau 999078, China
[2]Department of Electrical and Computer Engineering, Faculty of Science and Technology, University of Macau, Macau 999078, China
[3]Laboratory for Robotics and Engineering Systems, Institute for Systems and Robotics, Portugal
[4]Instituto Superior Técnico, Universidade de Lisboa, Portugal

Corresponding author: Pak Kin Wong (fstpkw@um.edu.mo)

This work was supported in part by the University of Macau Research Grant, under Grant MYRG-2016-00212-FST, Grant MYRG-2017-00135-FST, and Grant MYRG-2016-00097-FST, and in part by the Portuguese Fundação para a Ciência e a Tecnologia (FCT) through ISR under LARSyS UID/EEA/50009/2019.

ABSTRACT This paper addresses the problem of ride height tracking for an electronically-controlled active air suspension (AAS) system in the presence of parametric uncertainties and unmodeled dynamics. A mathematical model of a quarter vehicle with AAS system is first built on the basis of thermodynamics to describe the dynamic characteristics. Then, by employing the backstepping technique, a novel height tracking controller is proposed in order to guarantee that 1) the ride height of a vehicle can converge on a neighborhood of the desired height, achieving global uniform ultimate boundedness (GUUB); 2) the controller is robust to the parametric uncertainties by designing parameter estimators and introducing some conservativeness in the control law to dominate the unmodeled dynamics. Moreover, a group of smooth projectors is used to ensure all estimates remain within predefined corresponding bounds. To validate the efficiency and performance of the proposed strategy, the simulation and experimental results are presented and analyzed, showing that the proposed control strategy is superior to the PID controller and the recently proposed hybrid model predictive controller.

INDEX TERMS Active air suspension, pneumatic system, auto-mobile height control, robust control, parameter estimation.

I. INTRODUCTION

Controllable active air suspension (AAS) systems have been widely applied to improve the vehicle performance (ride comfort, road holding capacity and handling stability) by adjusting the vehicle ride height and level. The height of the vehicle sprung mass is adjusted by inflating and deflating the air spring to protect the vehicle body on rough roads, to reduce air drag, and to enhance safety during high-speed driving mode [1]–[4]. However, it is still a challenge to control the AAS robustly due to the fact that it is difficult to build a mathematical model that can be used to describe the dynamic characteristics of the AAS [4], [5], especially if we consider the fact that the adjustment of ride height usually changes the stiffness and hysteresis of the air spring caused by the aerothermodynamics, the behavior of the twisted cord rubber material of the air spring and the external disturbances [6]–[10].

The development of mathematical models for the AAS is an active research topic in the literature. For instance, the authors of [5] and [6] derived a nonlinear model for an air spring under the assumption that the working process of this air spring is adiabatic or isothermal. However, a linearised model is used for the stiffness of the air spring which is unable to capture the nonlinear nature of the spring dynamics. Further developments in [7] and [8], based on the aerothermodynamics fundamentals, yielded mathematical models of the air spring that appropriately describe the main characteristics

The associate editor coordinating the review of this manuscript and approving it for publication was Zhong Wu.

of stiffness and hysteresis. However, their models were developed without considering the dynamic characteristics caused by the behavior of the twisted cord rubber material of the air spring under the external disturbances. The authors of [9] conducted several experiments to analyze the twisted cord rubber material of the air spring with alternative cord angles and cord diameters for building a numerical model. However, this model was built using the finite element method, so it cannot be utilized for the ride height control (RHC) system. In [10], a dynamic model of an air spring was designed to investigate the dynamic behavior of an air spring suspension. However, this dynamic model does not consider the air variation in the air spring caused by inflation or deflating, so that it is also not suitable for the model-based RHC system. Therefore, the dynamic characteristics of the air spring as well as the external disturbances cannot be modeled exactly for RHC system in the existing literature, so they are classified as *unmodeled dynamics* and *parametric uncertainties* [11].

Apart from building an AAS model, the development of a ride height controller is also a challenge. Some researches have analyzed the control of a pneumatic system (AAS is one such system), such as the linear controllers presented in [12]–[14], but are not robust to *unmodeled dynamics*. The author of [4] developed a hybrid model predictive controller (HMPC) based on a linearized model to adjust the ride height. However, due to the highly nonlinear characteristics of the AAS, it is difficult to establish an accurate linearized model in the presence of the *parametric uncertainties* and *unmodeled dynamics* while guaranteeing the tracking performance under external disturbances. In order to overcome this weakness, several nonlinear controllers have been proposed. For example, the authors of [15] developed a self-tuning controller which can be used to improve the servo-control accuracy in the presence of highly nonlinear dynamics. However, their work is based on the assumption that the external force is constant which is not realistic for an actual test platform. The authors of [16] presented an adaptive neural network state feedback control approach, in which an adaptive radial basis function neural network was adopted to approximate uncertain non-linear functions in the dynamic suspension system. However, this neural network state observer is not effective in practice due to its long computation time.

By employing the sliding mode control (SMC) technique, nonlinear controllers were proposed in [14], [17]–[19], achieving asymptotic stability. However, the authors relax the matching condition for robustness in the existence of *unmodeled dynamics* and *parametric uncertainties* at the expense of high gain feedback, making the controllers prone to chattering. In order to avoid the chattering that affects sliding mode controllers, smoother techniques, such as backstepping, were employed for improving the tracking performance in [20]–[22], achieving local stability. Nonetheless, the proposed methodologies therein are not robust to *parametric uncertainties*, which are difficult to be measured and susceptible to change depending on the vehicle working conditions. In this respect, several estimation approaches are proposed in [23]–[26].

The objectives of this paper are to deal with the above issues, and the contributions and novelties of the paper are summarized as follows,

1) Building a mathematical model of the AAS for the multi-input-multi-output (MIMO) nonlinear model-based controller design. Unlike the linearized model derived in [5], [6], this model is able to describe the dynamic characteristics of the AAS by considering the *unmodeled dynamics* caused by the aerothermodynamics, behavior of the twisted cord rubber material of the air spring, and *parametric uncertainties* caused by the external disturbances;
2) Proposing a solution for the problem of height tracking in the presence of *parametric uncertainties* and unmodeled dynamics that drives the tracking error close to zero, achieving GUUB;
3) Designing parameter estimators through the use of a group of smooth projectors to ensure the estimates remain within predefined corresponding bounds, and introducing some conservativeness in the control law to dominate the *unmodeled dynamics* while guaranteeing robustness.
4) Designing an experimental platform of a solenoid-operated valve-controlled active air suspension (SOVCAAS) to validate the performance and robustness of the proposed controller. Experimental results are presented that validate the performance of the proposed control strategy.

For experimental tests, an in-house quarter car is used that is compact, low cost, low energy consumption and covers the tire nonlinearity and suspension geometry. The executive component of the pneumatic servo control system used herein is the solenoid-operated electro-pneumatic valve, in which the solenoid simply provides a fully open or fully closed position for the valve port. Compared with the proportional directional control valve, the solenoid-operated electro-pneumatic valve is more effective due to the application of the pulse width modulation (PWM) method [27], especially in the control of AAS systems [4], [17].

The remainder of this paper is structured as: In Section II, the notation used throughout this paper is introduced. Section III formulates a mathematical model for an active air suspension based on the first law of thermodynamics. In Section IV, a novel adaptive robust controller is designed based on the backstepping control technique. Section V-A shows simulation results and the comparison with the HMPC [4] which is the latest technique for RHC, and the PID controller. The experimental setup and experimental results are presented in Section VI-A and Section VI-B, respectively. Finally, Section VII summarizes the contents of this paper.

II. NOTATION

In this paper, $\mathbb{R}^n$ denotes the $n-$dimensional euclidean space. A function f is of class C^n if the derivatives $f', f'', \ldots, f^n$

exist and are continuous. For a vector $\mathbf{x} \in \mathbb{R}^n$, its norm is defined as $\|\mathbf{x}\| = \sqrt{\mathbf{x}^\mathsf{T}\mathbf{x}}$. A distinction between the partial derivative of a function with respect to a parameter, $f'(s) = (\partial f(s)/\partial s)$, and the total time derivative $\dot{f}(s(t)) = (\partial f(s)/\partial s)\dot{s}$ is made through the use of the prime ($'$) and overdot ($\dot{}$) operators. In addition, the unit vectors $\mathbf{n}_1$ and $\mathbf{n}_2$ are introduced as $\mathbf{n}_1 = [1,\ 0]^\mathsf{T}$, $\mathbf{n}_2 = [0,\ 1]^\mathsf{T}$. Throughout this paper, for a generic constant quantity $\mathbf{x} \in \mathbb{R}^n$, the estimate is denoted by $\hat{\mathbf{x}}$, the estimation error is $\tilde{\mathbf{x}} = \mathbf{x} - \hat{\mathbf{x}}$, and its dynamics verifies $\dot{\tilde{\mathbf{x}}} = -\dot{\hat{\mathbf{x}}}$, $\int_0^t \mathbf{x}\, d\tau$ denotes the integral of $\mathbf{x}$, and τ denotes the integration variable.

For the reader's reference, Table 1 features the main symbols and description pairs for the model, controller, and parameter estimators introduced in the sequel.

III. SYSTEM MODELING

To effectively achieve the RHC of the AAS and identify *parametric uncertainties*, it is necessary to gain a thorough understanding of the dynamic characteristics of the AAS system. A mathematical model of the AAS should be formulated first as a part of model-based controller design, and then the control action for inflating or deflating the adjustable air spring can be determined. The following assumptions are made to formulate a mathematical model of the air suspension system [17],

(1) The air is a perfect gas, and its kinetic energy is negligible in the AAS;
(2) The pressure and temperature of the air are homogeneous in the AAS;
(3) The process is polymorphic;
(4) The cross-sectional area of the AAS is constant;
(5) There is no air leakage in the AAS system components;
(6) The solenoid valve allows the air mass into or out of the air spring and is modeled by the static area-normalized mass flow equation (1), as shown at the bottom of this page, where $q(p_u, p_{dn})$ denotes the area-normalized mass flow rate between the high pressure source and the low pressure source, C_q is the deflating coefficient, γ is the specific heat ratio of air, R is the perfect gas constant, T is the air temperature, p_{dn} is the downstream pressure and p_u is the upstream pressure. The flow type depends on the pressure ratio (p_{dn}/p_u) and the critical pressure ratio p_{cr}.

Figure 1 shows the adjustable air spring in design-position and inflated position, including the states of the air. The flow of the air mass into or out of the control volume is controlled by operating the directional control valve. During the operation of the RHC, the difference of temperature between the inner and the outer sides of the control volume generates a heat transfer. In order to determine the energy interaction among the enclosed air inside the spring, the mounting elements and the control circuit environment, the adjustable air spring is divided into two control parts, Part I (inside of the red line) corresponds to the air volume enclosed in the air spring, and Part II (outside of the blue line) runs along the outer contour of the air spring. So the mounting elements and the rolling lobe are merged in one control system.

TABLE 1. Symbols.

Symbol	Description
$z_s\,(\mathrm{m})$	height of vehicle sprung mass
$z_u\,(\mathrm{m})$	unsprung mass displacement
$z_{as}\,(\mathrm{m})$	air spring displacement
$z_r\,(\mathrm{m})$	road disturbance
$b\,(\mathrm{N}\cdot\mathrm{s}\cdot\mathrm{m}^{-1})$	damping coefficient of damper
$p_{as}\,(\mathrm{Pa})$	air spring pressure
$p_0\,(\mathrm{Pa})$	initial air pressure
$p_s\,(\mathrm{Pa})$	pressure of high-pressure source
$p_{atm}\,(\mathrm{Pa})$	atmosphere pressure
$p_u\,(\mathrm{Pa})$	upstream pressure
$p_{dn}\,(\mathrm{Pa})$	downstream pressure
p_{cr}	critical pressure ratio
$v_{as}\,(\mathrm{m}^3)$	air spring volume
$T_{as}\,(\mathrm{K})$	air spring temperature
$\dot{Q}\,(\mathrm{J}\cdot\mathrm{s}^{-1})$	heat transfer rate
n	polytropic index
$m_s\,(\mathrm{kg})$	sprung mass of quarter vehicle
$m_u\,(\mathrm{kg})$	unsprung mass of quarter vehicle
$m_{as}\,(\mathrm{kg})$	air mass inside air spring
$\dot{m}_{des}\,(\mathrm{kg}\cdot\mathrm{s}^{-1})$	desired air mass change
$\dot{m}_{in}\,(\mathrm{kg}\cdot\mathrm{s}^{-1})$	inflating air mass rate
$\dot{m}_{out}\,(\mathrm{kg}\cdot\mathrm{s}^{-1})$	deflating air mass rate
$x_d\,(\mathrm{m})$	desired height
$k_t\,(\mathrm{N}\cdot\mathrm{m}^{-1})$	tire stiffness
$T_p\,(\mathrm{s})$	PWM signal period
$q_{LD}\,(\mathrm{P_a}\cdot\mathrm{s}^{-1})$	defined virtual control input
C_q	deflating coefficient
$D_c\,(\%)$	duty cycle of PWM signal
$S_x\,(\mathrm{m}^2)$	solenoid valve orifice open area
u	actuator command
$q(p_u, p_{dn})\,(\mathrm{kg}\cdot\mathrm{s}^{-1})$	area-normalized mass flow rate
f_n, d_n	parametric uncertainties
f_0, d_0	unmodeled dynamics

$$q(p_u, p_{dn}) = \begin{cases} \sqrt{\dfrac{2\gamma}{R(\gamma-1)}}\sqrt{\left(\dfrac{p_{dn}}{p_u}\right)^{\frac{2}{\gamma}} - \left(\dfrac{p_{dn}}{p_u}\right)^{\frac{\gamma+1}{\gamma}}}\dfrac{C_q p_u}{\sqrt{T}}, & \text{if } \left(\dfrac{p_{dn}}{p_u}\right) \geq p_{cr} \text{ (unchoked)} \\ \sqrt{\dfrac{\gamma}{R}\left(\dfrac{2}{\gamma+1}\right)^{\frac{\gamma+1}{\gamma-1}}}\dfrac{C_q p_u}{\sqrt{T}}, & \text{if } \left(\dfrac{p_{dn}}{p_u}\right) < p_{cr} \text{ (choked)} \end{cases} \tag{1}$$

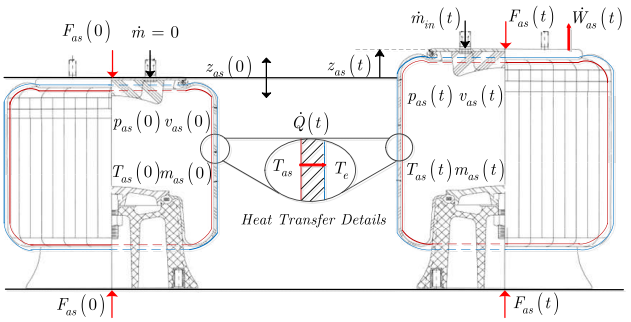

FIGURE 1. System borders of control volume of adjustable air spring.

The balance of the internal energy is modeled by the first law of thermodynamics [7], and the flow rate of air mass into or out of the control volume is viewed as a control input that is expressed by Equation 1. In this case, the model of the air spring is expressed as

$$\dot{Q}+\dot{H}=\dot{U}+\dot{W}_{as}, \tag{2}$$

where $\dot{Q}$ denotes the heat transfer rate between the inner and the outer sides of the control volume, which is given by

$$\dot{Q}=h_t A_{heat}(T_e-T_{as}), \tag{3}$$

where h_t is the heat transfer coefficient, A_{heat} represents the area of the heat transfer, T_e and T_{as} are temperatures of the outer and the inner sides of the control volume, respectively. And $\dot{H}$ denotes the energy change caused by the air mass transfer, which is expressed as

$$\dot{H}=c_p T_e\dot{m}_{in}-c_p T_{as}\dot{m}_{out}, \tag{4}$$

with c_p is the specific heat at constant pressure, $\dot{m}_{in}$ represents the increment of the air mass in the air spring, and $\dot{m}_{out}$ denotes the decrement of the air mass in the air spring. The time derivative of the internal energy of the air spring control volume is defined by

$$\dot{U}=c_v(\dot{m}_{in}-\dot{m}_{out})T_{as}. \tag{5}$$

Moreover, $\dot{W}_{as}$ denotes the change of the power that is performed on the control volume, and is defined as

$$\dot{W}_{as}=-p_{as}\dot{v}_{as}. \tag{6}$$

To derive the pressure dynamic equation from (2), the temperature inside the control volume is replaced with the pressure inside the control volume using the following ideal gas law

$$p_{as}v_{as}=m_{as}RT_{as}. \tag{7}$$

The derivative of the temperature inside the control volume with respect to time can be derived by differentiating Equation (7) with respect to time as follows

$$\frac{dT_{as}}{dt}\frac{1}{T_{as}}=\frac{dp_{as}}{dt}\frac{1}{p_{as}}+\frac{dv_{as}}{dt}\frac{1}{v_{as}}-\frac{dm_{as}}{dt}\frac{1}{m_{as}}, \tag{8}$$

where T_{as} is the air temperature, p_{as} denotes the air pressure, v_{as} represents the air volume and m_{as} is the air mass inside the control volume. The mass m_0 denotes the initial air mass inside the control volume and it varies with the air mass flowing into $\dot{m}_{in}$ and out $\dot{m}_{out}$ of the control volume on the basis of the mass conservation as follows

$$m_{as}=m_0+\int_0^t(\dot{m}_{in}-\dot{m}_{out})\,d\tau. \tag{9}$$

Combining (2), (8) and (9), the first order differential equation for the temperature and pressure of the air in the control volume can be expressed as,

$$\begin{cases}\dot{T}_{as}= & \frac{RT_{as}(\gamma T_e-T_{as})}{p_{as}v_{as}}\dot{m}_{in}-\frac{RT_{as}^2(\gamma-1)}{p_{as}v_{as}}\dot{m}_{out}\\ & +\frac{T_{as}(1-\gamma)}{v_{as}}\dot{v}_{as}+\frac{T_{as}(\gamma-1)}{p_{as}v_{as}}\dot{Q}\\ \dot{p}_{as}= & \frac{\gamma R}{v_{as}}(\dot{m}_{in}T_e-\dot{m}_{out}T_{as})-\frac{\gamma T_{as}}{v_{as}}\dot{v}_{as}\\ & +\frac{\gamma-1}{v_{as}}\dot{Q}\end{cases} \tag{10}$$

where $\gamma=c_p/c_v$ denotes the specific heat ratio, and $R/c_v=\gamma-1$. Equation (10) represents the exact higher-order model of the air spring, however the gas temperature inside the air spring cannot be measured. Nonetheless, the influence of heat transfer coefficient between Part I and Part II can be assessed by using a reduced model [28]. Additionally, considering the gas to follow the polymorphic process leads to the following reduced model,

$$\begin{cases}T_{as}= & T_e\left(\frac{p_s}{p_0}\right)^{\frac{n-1}{n}}\\ \dot{p}_{as}= & \frac{\gamma R}{v_{as}}(\dot{m}_{in}T_e-\dot{m}_{out}T_{as})-\frac{\gamma p_{as}}{v_{as}}\dot{v}_{as}\\ & +\frac{\gamma-1}{v_{as}}\dot{Q}\end{cases} \tag{11}$$

where p_0 is the initial air pressure when the air spring is at the design-position, p_s is the pressure of high-pressure source, n is the polytropic index with a mean value of 1.35. The adjustable air spring force can be obtained as,

$$F_{as}=(p_{as}-p_{atm})A_{as} \tag{12}$$

where F_{as} is the force, through which the pressure inside the air spring is transformed into the force, and p_{atm} is the atmosphere pressure. Under the assumption that the damper is linear, a quarter vehicle model with AAS, displayed in Figure 2, is modeled as,

$$\begin{cases}z_{as}=z_s-z_u\\ m_s\ddot{z}_s=F_{as}-b\dot{z}_{as}-m_s g\\ m_u\ddot{z}_u=k_t(z_r-z_u)-F_{as}+b\dot{z}_{as}\end{cases} \tag{13}$$

where b is the damping coefficient of the damper, m_s is the sprung mass of a quarter vehicle, m_u is the unsprung mass of a quarter vehicle, k_t is the tire stiffness, z_r is the road disturbance, and z_u and z_s are the displacements of the unsprung mass and the sprung mass of the quarter vehicle, respectively. In the AAS system, the highly nonlinear characteristics of the air spring as well as the external disturbances

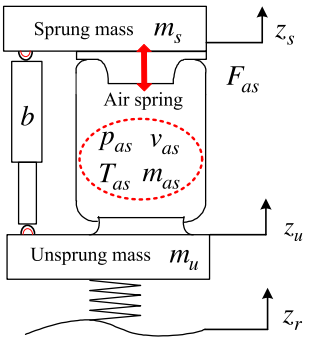

FIGURE 2. Quarter vehicle model with active air suspension.

cannot be modeled exactly, so they are classified as *parametric uncertainties* and *unmodeled dynamics*. For the sake of simplicity, the quarter vehicle model with an AAS determined by Equations (10), (11), (12), and (13), can be written in a compact state-space form as

$$\begin{aligned}\dot{x}_1 &= x_2, \dot{x}_2 = \frac{1}{m_s}(\bar{A}_{as}(x_3 - p_{atm}) - b(x_2 - \dot{z}_u) - m_s g + f_n + f_0),\\ \dot{x}_3 &= \frac{\gamma R}{s_p v_{as}}(\dot{m}_{in} T_e - \dot{m}_{out} T_{as}) - \frac{\gamma A_{as}}{v_{as}} x_2 x_3\\ &\quad + \frac{\gamma - 1}{s_p v_{as}}\dot{Q} + d_n + d_0. \end{aligned} \tag{14}$$

where $x_1 = z_s$, $x_2 = \dot{z}_s$, $x_3 = p_{as}/s_p$, z_s denotes the displacement of the sprung mass of the quarter vehicle, $s_p = 10^5$, $\bar{A}_{as} = A_{as} s_p$ is the effective area of the adjustable air spring. In addition, m_s denotes the sprung mass of the quarter vehicle, T_{as} is the air temperature, v_{as} is the air volume, $\dot{Q}$ is the heat transfer rate between the inner and the outer sides of the control volume, b denotes the damping coefficient, $(f_n + f_0(t))$ are the lumped modeling errors of the state variable of $\ddot{z}_s$, including *parametric uncertainties* caused by the external disturbances and *unmodeled dynamics* caused by the aerothermodynamics and behavior of the twisted cord rubber material of the air spring, and f_n denotes its nominal value. $(d_n + d_0(t))$ are the lumped modeling errors of the state variable of $\dot{p}_{as}/s_p$, including *parametric uncertainties* caused by the external disturbances and *unmodeled dynamics* caused by the aerothermodynamics and behavior of the twisted cord rubber material of the air spring, and d_n represent its nominal value [26]. Moreover, we make the following two assumptions as,

Assumption 1: Under the same vertical excitation, the damping coefficient b, nominal values f_n and d_n are constant, uncertain, and satisfy

$$|b| \le \kappa_1, \quad |f_n| \le \kappa_2, \quad |d_n| \le \kappa_3 \tag{15}$$

where κ_1, κ_2 and κ_3 are known positive numbers.

Assumption 2: Unmodeled dynamics $f_0(t)$ and $d_0(t)$ satisfy

$$|f_0(t)| \le f_{\max}, \quad |d_0(t)| \le d_{\max} \tag{16}$$

for all $t \ge 0$, where $f_{\max}$ and $d_{\max}$ are known positive numbers which can be determined through the experimental test of the corresponding hardware components.

It is crucial to point out that Assumption 1 is unrealistic in practice because the values are not exactly constant and difficult to be measured precisely, in general, they are slowly changing quantities. Therefore, it is a convenient starting point for us to improve the stability of the AAS system even if they are not exactly constant.

Furthermore, in order to highlight the linear dependence on the *parametric uncertainties*, the dynamic equations for $\dot{x}_2$ and $\dot{x}_3$ can be rewritten more compactly as

$$\dot{x}_2 = \frac{1}{m_s}(\bar{A}_{as}(x_3 - p_{atm}) - m_s g + \mathbf{\Phi}(x_2, \dot{z}_u)\boldsymbol{\theta}_{x2} + f_0) \tag{17}$$

$$\dot{x}_3 = q_{LD} - \frac{\gamma A_{as}}{v_{as}} x_2 x_3 + \frac{\gamma - 1}{s_p v_{as}}\dot{Q} + \theta_{x3} + d_0 \tag{18}$$

where $\mathbf{\Phi}(x_2, \dot{z}_u) = [-(x_2 - \dot{z}_u),\ 1]$, $\boldsymbol{\theta}_{x2} = [b,\ f_n]^{\mathsf{T}}$, $\theta_{x3} = d_n$, and $q_{LD} = \gamma R(\dot{m}_{in} T_e - \dot{m}_{out} T_{as})/(s_p v_{as})$ is viewed as the virtual control input.

IV. CONTROLLER DESIGN

In this section, we consider the problem of height tracking in the presence of *parametric uncertainties* and *unmodeled dynamics*, stated as: let $x_d(t) \in \mathbb{R}$ denotes the desired height, which is a curve of class at least $\mathcal{C}^3$ (the derivatives of $\dot{x}_d(t)$, $\ddot{x}_d(t)$ and $x_d^{(3)}(t)$ exist and are continuous) and its time derivatives are bounded. The control objective of this problem is to design a control law for the virtual control input of the AAS that guarantees the convergence of the ride height on a neighborhood of the desired height. Moreover, it is important to point out that when there is a change of mode (desired height is changed), the controller can be viewed as the restart with different initial conditions.

To solve the height tracking problem, we start by denoting the position error as

$$e_1 = x_1 - x_d, \tag{19}$$

and consider an initial Lyapunov function candidate given by

$$V_1 = \frac{1}{2}e_1^2, \tag{20}$$

whose time derivative yields

$$\dot{V}_1 = e_1(\dot{x}_1 - \dot{x}_d). \tag{21}$$

Isolating a negative definite term in e_1 and rearranging the terms of $\dot{V}_1$, we get

$$\dot{V}_1 = -k_1 e_1^2 + e_1(\dot{x}_1 - \dot{x}_d + k_1 e_1). \tag{22}$$

Following the backstepping technique, we define the new error e_2 as

$$e_2 = \dot{x}_1 - \dot{x}_d + k_1 e_1, \tag{23}$$

and rewrite (22), we have

$$\dot{V}_1 = -k_1 e_1^2 + e_1 e_2. \tag{24}$$

Constructing a new Lyapunov function candidate by incorporating e_2, we obtain

$$V_2 = \frac{1}{2}e_1^2 + \frac{1}{2}m_s e_2^2, \tag{25}$$

with time derivative

$$\dot{V}_2 = -k_1 e_1^2 - k_2 e_2^2 + e_2\Big(\bar{A}_{as}(x_3 - p_{atm}) - m_s g + f_0 + \mathbf{\Phi}(x_2, \dot{z}_u)\boldsymbol{\theta}_{x2} - m_s\ddot{x}_d + k_1 m_s \dot{e}_1 + k_2 e_2 + e_1\Big). \tag{26}$$

Furthermore, we can rewrite (26) as

$$\begin{aligned}\dot{V}_2 &\leq -W_1 + e_2\Big(\bar{A}_{as}x_3 - \bar{A}_{as}p_{atm} - m_s g + \mathbf{\Phi}(x_2, \dot{z}_u)\boldsymbol{\theta}_{x2} - m_s\ddot{x}_d + k_1 m_s \dot{e}_1 + k_2 e_2 + e_1\Big) + |e_2 f_0| \\ &\leq -W_1 + e_2\Big(\bar{A}_{as}x_3 - \bar{A}_{as}p_{atm} - m_s g + \mathbf{\Phi}(x_2, \dot{z}_u)\boldsymbol{\theta}_{x2} - m_s\ddot{x}_d + k_1 m_s \dot{e}_1 + k_2 e_2 + e_1\Big) + |e_2 f_{\max}|,\end{aligned} \tag{27}$$

where $W_1 = k_1 e_1^2 + k_2 e_2^2$ is positive definite. Following [29], the inequality

$$|\chi| - \chi \tanh\left(\frac{\chi}{\epsilon}\right) \leq 0.2785\epsilon \tag{28}$$

is used, where ϵ is a positive number that can be chosen arbitrarily small. We have

$$|e_2 f_{\max}| \leq e_2 f_{\max} \tanh\left(\frac{e_2 f_{\max}}{\epsilon_1}\right) + 0.2785\epsilon_1, \tag{29}$$

then, Equation (27) can be further rewritten as

$$\begin{aligned}\dot{V}_2 \leq -W_1 + e_2\Big(&\bar{A}_{as}x_3 - \bar{A}_{as}p_{atm} - m_s g + \mathbf{\Phi}(x_2, \dot{z}_u)\boldsymbol{\theta}_{x2} \\ &- m_s\ddot{x}_d + k_1 m_s \dot{e}_1 + k_2 e_2 + e_1 + f_{\max}\tanh\left(\frac{e_2 f_{\max}}{\epsilon_1}\right)\Big) \\ &+ 0.2785\epsilon_1.\end{aligned} \tag{30}$$

It is noted that the *parametric uncertainties* $\boldsymbol{\theta}_{x2}$ cannot be included in the control law. As such, we introduce estimates for these quantities, as $\hat{\boldsymbol{\theta}}_{x2}$. For a generic constant quantity $x \in \mathbb{R}^n$, the estimate is denoted by $\hat{x}$, the estimation error is $\tilde{x} = x - \hat{x}$, and its rate of change is $\dot{\tilde{x}} = -\dot{\hat{x}}$. The new Lyapunov function candidate featuring the estimation errors $\tilde{\boldsymbol{\theta}}_{x2}$ is then

$$V_{2b} = V_2 + \frac{1}{2}\tilde{\boldsymbol{\theta}}_{x2}^{\mathsf{T}}\Lambda_1^{-1}\tilde{\boldsymbol{\theta}}_{x2}, \tag{31}$$

with time derivative

$$\begin{aligned}\dot{V}_{2b} \leq -W_1 + e_2\Big(&\bar{A}_{as}x_3 - \bar{A}_{as}p_{atm} - m_s g + \mathbf{\Phi}(x_2, \dot{z}_u)\hat{\boldsymbol{\theta}}_{x2} \\ &- m_s\ddot{x}_d + k_1 m_s \dot{e}_1 + k_2 e_2 + e_1 + f_{\max}\tanh\left(\frac{e_2 f_{\max}}{\epsilon_1}\right)\Big) \\ &+ 0.2785\epsilon_1 + \tilde{\boldsymbol{\theta}}_{x2}^{\mathsf{T}}\Big(\mathbf{\Phi}(x_2, \dot{z}_u)^{\mathsf{T}} e_2 - \Lambda_1^{-1}\dot{\hat{\boldsymbol{\theta}}}_{x2}\Big),\end{aligned} \tag{32}$$

where the estimation gain $\Lambda_1 = \text{diag}(\lambda_1, \lambda_2)$ is a positive definite diagonal matrix. Letting h be the collection of measurable and known terms given by

$$\begin{aligned}h = -\bar{A}_{as}p_{atm} - m_s g + \mathbf{\Phi}(x_2, \dot{z}_u)\hat{\boldsymbol{\theta}}_{x2} - m_s\ddot{x}_d + k_1 m_s \dot{e}_1 \\ + k_2 e_2 + e_1 + f_{\max}\tanh\left(\frac{e_2 f_{\max}}{\epsilon_1}\right),\end{aligned} \tag{33}$$

and rearranging terms, $\dot{V}_{2b}$ becomes

$$\begin{aligned}\dot{V}_{2b} \leq -W_1 + e_2\Big(\bar{A}_{as}x_3 + h\Big) + 0.2785\epsilon_1 \\ + \tilde{\boldsymbol{\theta}}_{x2}^{\mathsf{T}}\Big(\mathbf{\Phi}(x_2, \dot{z}_u)^{\mathsf{T}} e_2 - \Lambda_1^{-1}\dot{\hat{\boldsymbol{\theta}}}_{x2}\Big).\end{aligned} \tag{34}$$

Even though the *parametric uncertainties* are assumed to be bounded, a straightforward implementation of estimators, such as setting

$$\dot{\hat{b}} = \lambda_1\Big(\mathbf{n}_1\mathbf{\Phi}(x_2, \dot{z}_u)^{\mathsf{T}} e_2\Big), \tag{35}$$

can lead to wind-up phenomena and result in unbounded growth of the estimates. Therefore, in order to ensure the estimations remain within an *a prior* bounded set, and are sufficiently smooth for continuing the backstepping process, a smooth projection operator is employed [30], [31]. The projection is given by

$$\mathbf{Proj}(\boldsymbol{\mu}, \hat{\mathbf{s}}) = \boldsymbol{\mu} - \frac{\eta_1\eta_2}{2(\varsigma^2 + 2\varsigma B)^{n+1}B^2}\hat{\mathbf{s}}, \tag{36}$$

where $\boldsymbol{\mu}$ is the variable to be projected and $\hat{\mathbf{s}}$ denotes the estimate of $\mathbf{s}$. The parameters are defined as

$$\eta_1 = \begin{cases}(\hat{\mathbf{s}}^{\mathsf{T}}\hat{\mathbf{s}} - B^2)^{n+1} & (\hat{\mathbf{s}}^{\mathsf{T}}\hat{\mathbf{s}} - B^2) > 0, \\ 0 & \text{otherwise},\end{cases} \tag{37}$$

$$\eta_2 = \hat{\mathbf{s}}^{\mathsf{T}}\boldsymbol{\mu} + \sqrt{(\hat{\mathbf{s}}^{\mathsf{T}}\boldsymbol{\mu})^2 + \delta^2}, \tag{38}$$

where ς, δ are arbitrarily positive parameters, and B is the upper bound of $||\mathbf{s}||$. This projection has the following important properties

1) $||\hat{\mathbf{s}}|| \leq B + \varsigma, \forall t \geq 0$
2) $\tilde{\mathbf{s}}^{\mathsf{T}}\,\mathbf{Proj}(\boldsymbol{\mu}, \hat{\mathbf{s}}) \geq \tilde{\mathbf{s}}^{\mathsf{T}}\boldsymbol{\mu}$
3) $||\mathbf{Proj}(\boldsymbol{\mu}, \hat{\mathbf{s}})|| \leq ||\boldsymbol{\mu}||(1 + ((B + \varsigma)/B)^2) + (B + \varsigma)\delta/(2B^2)$
4) $\mathbf{Proj}(\boldsymbol{\mu}, \hat{\mathbf{s}})$ is of class $\mathcal{C}^n$.

The estimate updating laws for $\dot{\hat{b}}$ and $\dot{\hat{f}}_n$ are set as

$$\dot{\hat{b}} = \lambda_1\mathbf{Proj}(\mathbf{n}_1\mathbf{\Phi}(x_2, \dot{z}_u)^{\mathsf{T}} e_2, \hat{b}), \tag{39}$$

$$\dot{\hat{f}}_n = \lambda_2\mathbf{Proj}(\mathbf{n}_2\mathbf{\Phi}(x_2, \dot{z}_u)^{\mathsf{T}} e_2, \hat{f}_n), \tag{40}$$

which ensures, by Property (2) of the projector that

$$\mathbf{\Phi}(x_2, \dot{z}_u)^{\mathsf{T}} e_2 - \Lambda_1^{-1}\dot{\hat{\boldsymbol{\theta}}}_{x2} \leq 0 \tag{41}$$

with $\mathbf{n}_1 = [1,\ 0], \mathbf{n}_2 = [0,\ 1]$. Substituting (39) and (40) into (34), $\dot{V}_{2b}$ becomes

$$\dot{V}_{2b} \leq -W_1 + e_2\Big(\bar{A}_{as}x_3 + h\Big) + 0.2785\epsilon_1. \tag{42}$$

Continuing with the backstepping process, we define the last error term as

$$e_3 = \bar{A}_{as}x_3 + h, \tag{43}$$

and augment the Lyapunov function candidate as

$$V_3 = V_{2b} + \frac{1}{2}e_3^2. \tag{44}$$

The closed-loop time derivative is then

$$\dot{V}_3 \leq -W_2 + e_3\Big(e_2 + \bar{A}_{as}\Big(q_{LD} - \frac{\gamma A_{as}}{v_{as}}x_2x_3 + \frac{\gamma-1}{s_p v_{as}}\dot{Q} + \theta_{x3} + d_0\Big) + \dot{h} + k_3e_3\Big) + 0.2785\epsilon_1. \quad (45)$$

where $W_2 = W_1 + k_3e_3^2$.

Here, we notice that apart from the *parametric uncertainties* $\boldsymbol{\theta}_{x2}$ and θ_{x3}, the time derivative $\dot{V}_3$ is also dependent on the *unmodeled dynamics* d_0 and f_0 through the dependency of $\dot{h}$ in these quantities. In order to simplify the dynamic presentation and exploit the linear dependency of x_2 in the uncertain quantities, the time derivative $\dot{h}$ can be expressed as

$$\dot{h} = \hat{\dot{h}} + \frac{\partial h}{\partial \dot{x}_2}\Big(\boldsymbol{\Phi}(x_2, \dot{z}_u)\tilde{\boldsymbol{\theta}}_{x22} + f_0\Big), \quad (46)$$

where $\hat{\boldsymbol{\theta}}_{x22}$ is introduced as new estimate for $\boldsymbol{\theta}_{x2}$ and $\tilde{\boldsymbol{\theta}}_{x22}$ is the estimation error. The symbol $\hat{\dot{h}}$ is the estimate for $\dot{h}$ obtained by using the new estimate $\hat{\boldsymbol{\theta}}_{x22}$ for the *parametric uncertainties*. The second term in Equation (46) is therefore the estimate error. We now establish the final Lyapunov function candidate by adding the terms of parameter estimate error to V_3 as follows,

$$V_{3b} = V_3 + \frac{1}{2}\tilde{\boldsymbol{\theta}}_{x22}\Lambda_2^{-1}\tilde{\boldsymbol{\theta}}_{x22} + \frac{1}{2\lambda_5}\tilde{\theta}_{x3}^2, \quad (47)$$

where the estimate gain $\Lambda_2 = \text{diag}(\lambda_3, \lambda_4)$ is a positive definite diagonal matrix and λ_5 is also a positive constant. Computing the time derivative of V_{3b}, we obtain

$$\begin{aligned}\dot{V}_{3b} \leq\ & -W_2 + e_3\Big(e_2 + \bar{A}_{as}\Big(q_{LD} - \frac{\gamma A_{as}}{v_{as}}x_2x_3 \\ & + \frac{\gamma-1}{s_p v_{as}}\dot{Q} + \hat{\theta}_{x3} + d_{\max}\tanh\Big(\frac{e_3\bar{A}_{as}d_{\max}}{\epsilon_2}\Big)\Big) \\ & + \hat{\dot{h}} + k_3e_3 + \frac{\partial h}{\partial \dot{x}_2}f_{\max}\tanh\Big(\frac{\partial h}{\partial \dot{x}_2}\frac{e_3 f_{\max}}{\epsilon_3}\Big)\Big) \\ & + \tilde{\boldsymbol{\theta}}_{x22}^{\mathsf{T}}\Big(e_3\frac{\partial h}{\partial \dot{x}_2}\boldsymbol{\Phi}(x_2, \dot{z}_u) - \Lambda_2^{-1}\dot{\hat{\boldsymbol{\theta}}}_{x22}\Big) \\ & + \tilde{\theta}_{x3}\Big(e_3\bar{A}_{as} - \frac{1}{\lambda_5}\dot{\hat{\theta}}_{x3}\Big) + 0.2785\sum_{i=1}^{3}\epsilon_i. \end{aligned} \quad (48)$$

Choosing the virtual control law for q_{LD} as

$$\begin{aligned} q_{LD} = & -\frac{1}{\bar{A}_{as}}\Big(e_2 + \frac{\partial h}{\partial \dot{x}_2}f_{\max}\tanh\Big(\frac{\partial h}{\partial \dot{x}_2}\frac{e_3 f_{\max}}{\epsilon_3}\Big) \\ & + \hat{\dot{h}} + k_3e_3\Big) + \frac{\gamma A_{as}}{v_{as}}x_2x_3 - \frac{\gamma-1}{s_p v_{as}}\dot{Q} - \hat{\theta}_{x3} \\ & - d_{\max}\tanh\Big(\frac{e_3\bar{A}_{as}d_{\max}}{\epsilon_2}\Big), \end{aligned} \quad (49)$$

and the estimating laws for $\dot{\hat{b}}_2$, $\dot{\hat{f}}_{n2}$ and $\dot{\hat{\theta}}_{x3}$,

$$\dot{\hat{b}}_2 = \lambda_3\mathbf{Proj}(\mathbf{n}_1 e_3\frac{\partial h}{\partial \dot{x}_2}\boldsymbol{\Phi}(x_2, \dot{z}_u), \hat{b}_2), \quad (50)$$

$$\dot{\hat{f}}_{n2} = \lambda_4\mathbf{Proj}(\mathbf{n}_2 e_3\frac{\partial h}{\partial \dot{x}_2}\boldsymbol{\Phi}(x_2, \dot{z}_u), \hat{f}_{n2}), \quad (51)$$

$$\dot{\hat{\theta}}_{x3} = \lambda_5\mathbf{Proj}(e_3\bar{A}_{as}, \hat{\theta}_{x3}). \quad (52)$$

Moreover, it is important to point out that in (39) and (50), the value of B in (36) is κ_1. In (40) and (51), the value of B is κ_2. In (52), the value of B equals to κ_3. In sum, the value of B is changed according to the actual maximum value of the unknown parameter needed to be estimated.

Substituting (49), (50), (51) and (52) into (48), in closed-loop, we have

$$\dot{V}_{3b} \leq -W_2 + 0.2785\sum_{i=1}^{3}\epsilon_i. \quad (53)$$

where $W_2 = k_1e_1^2 + k_2e_2^2 + k_3e_3^2$ is positive definite.

In summary, the main result of height tracking problem is stated as

Theorem 1: Let the model of the active air suspension system be described by (14) *and* $x_d \in \mathcal{C}^3$ *be the desired height. Considering the closed-loop obtained by the following control law* (49)*, and the adaptive estimation laws* (39)*,* (40)*,* (50)*,* (51) *and* (52) *for any initial condition, the tracking errors* (e_1, e_2, e_3)*, given by* (19)*,* (23) *and* (43)*, can converge on a ball origin with arbitrarily small radius, achieving GUUB.*

Proof: Going back to (53), notice that $\dot{V}_{3b}$, in closed-loop, can be upper bounded by

$$\begin{aligned}\dot{V}_{3b} &\leq -k_1e_1^2 - k_2e_2^2 - k_3e_3^2 + 0.2785\sum_{i=1}^{3}\epsilon_i \\ &\leq -\lambda_{\min}\mathbf{x}^{\mathsf{T}}\mathbf{x} + 0.2785\sum_{i=1}^{3}\epsilon_i \end{aligned} \quad (54)$$

where $\lambda_{\min} = \min(k_1, k_2, k_3)$ and $\mathbf{x} = [e_1, e_2, e_3]^{\mathsf{T}}$, which is strictly negative for

$$||\mathbf{x}|| > \delta = \sqrt{\frac{0.2785\sum_{i=1}^{3}\epsilon_i}{\lambda_{\min}}}. \quad (55)$$

It follows that $||\mathbf{x}||$ is ultimately bounded by δ which can be made arbitrarily small by adjusting the values of k_1, k_2, k_3 and ϵ_i. □

Remark 1: With respect to the role of ϵ_i*, it is noted that from Theorem 1, we conclude that for the same gains, smaller* ϵ_i *leads to smaller final position error. In light of this consideration, it seems that we should choose* ϵ_i *as small as possible. Nonetheless, since the input* q_{LD} *relies on the inverse of* ϵ_i*, a smaller* ϵ_i *could lead to* ϵ_i *becoming more sensitive to* e_1*,* e_2 *and* e_3*. As a consequence, unwanted oscillation could arise. Similarly, we cannot choose gains* k_1*,* k_2*,* k_3 *as large as possible. In summary, we need to find a trade-off between the amplitude of oscillation and tracking accuracy.*

V. SIMULATION STUDY

A. SIMULATION

In order to verify the effectiveness of the proposed controller, a co-simulation is conducted in this section by combining the virtual plant of SOVCAAS in AMESim software with the proposed controller in MatLab/Simulink to adjust the

ride height of a quarter vehicle. The RHC is performed by a frequent air inflating and deflating of the air spring in order to track the desired height. The main objectives of the RHC are to facilitate passenger entry/exit, reduce the air drag on the vehicle, improve the ride comfort, and driving safety. The operation modes of the air suspension include easy entry mode, normal mode, highway mode and off-road mode [17]. When there is a change of the desired modes, the controller presented in Section IV is restarted with different initial conditions so as to track its corresponding desired height.

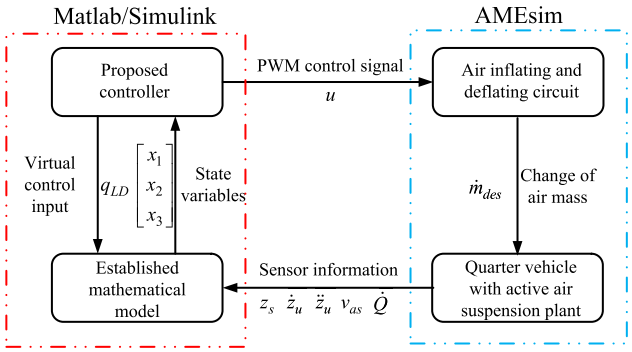

FIGURE 3. Control block diagram of co-simulation.

TABLE 2. Parameter used in simulation.

Parameter	Value	Parameter	Value
A_{as}	$178\,\mathrm{mm}^2$	d_{max}	2×10^{-2}
A_{heat}	$500\,\mathrm{J\cdot m^{-2}\cdot K^{-1}\cdot s^{-1}}$	f_{max}	0.2
b	$1140\mathrm{N\cdot s\cdot m^{-1}}$	k_1	3
g	$9.8\,\mathrm{m\cdot s^{-2}}$	k_2	450
h_t	1×10^{-2}	k_3	50
m_s	300 kg	λ_1	2.35×10^4
m_u	30 kg	λ_2	1
V_t	8 L	λ_3	5.5×10^2
p_0	5.11 Bar	λ_4	-0.8×10^{-3}
p_{atm}	1.01 Bar	λ_5	0.1×10^{-4}
z_0	0.204 m	ϵ_1	1×10^{-2}
S_x	$2\times10^{-5}\,\mathrm{m}^2$	ϵ_2	1×10^{-2}
C_q	8×10^{-2}	ϵ_3	1×10^{-2}

A virtual plant of a quarter vehicle with AAS system is established by using the toolboxes provided by AMESim. The mathematical model of the AAS and the proposed controller are designed and programmed in MatLab/Simulink. Figure 3 shows the control block diagram of the co-simulation. Different from the mathematical model of the proposed controller implemented in MatLab/Simulink, the AMESim-based virtual plant is established based on the actual system configuration. The major parameters of the air suspension and the vehicle used in the co-simulation are given in Table 2. It is noteworthy that the parameters b, f_n and d_n are assumed to be known and used in the virtual plant only. The virtual plant can be viewed as a real vehicle with an AAS system and those parameters are uncertain in practice. In this section, the estimators developed to demonstrate how to approximate the practically uncertain parameters.

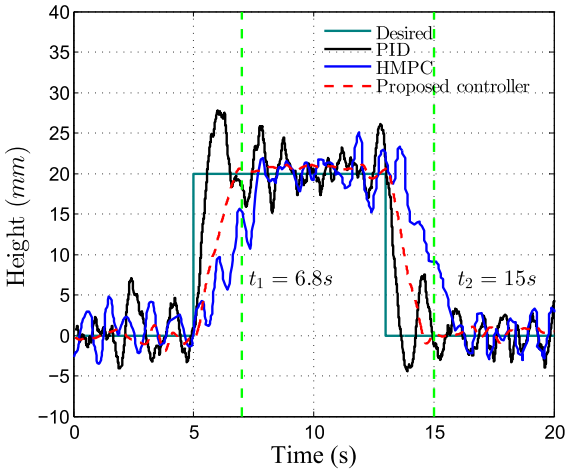

FIGURE 4. Height of SOVCAAS on a quarter vehicle in co-simulation.

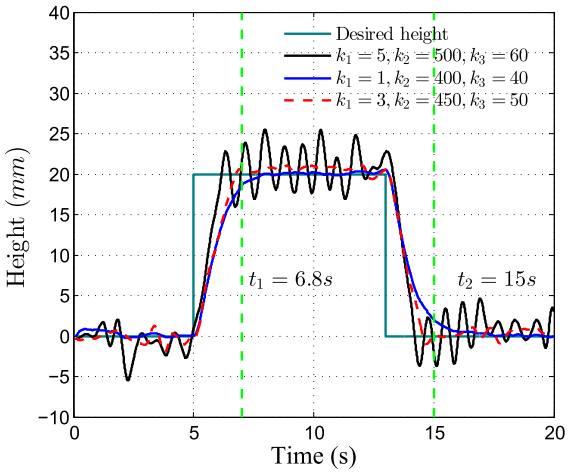

FIGURE 5. Performance comparison of SOVCAAS on a quarter vehicle in co-simulation.

B. SIMULATION RESULTS

The simulation is conducted under the condition of a rough road corresponding to the class B of ISO road profile (which is a standard random road profile) and a driving speed of $50\,\mathrm{km\cdot h^{-1}}$ [32]. Figure 4 shows that the ride height of the virtual plant with the proposed controller can track the desired value within 3 s during both leveling up (time from 5 s to t_1) and lowering down (time from 13 s to t_2) processes. As presented in Remark 1, the tracking error can be decreased by increasing the values of k_1, k_2, k_3 from a theoretical point of view. However, large gains will cause oscillation. Figure 5 plots the tracking performance of the proposed controller with three sets of gain values. It is also necessary to choose a set of suitable gains for the closed-loop RHC system, which can effectively improve the tracking accuracy while guaranteeing a tolerable amplitude of oscillation. Based on Figure 5, the set of gain values ($k_1 = 3$, $k_2 = 450$ and $k_3 = 50$) is selected as shown in Table 2.

Compared with the pressure of the air spring simulated by the virtual air suspension (i.e. virtual plant), the maximum error of the air pressure is 0.22 bar as shown in Figure 6, from

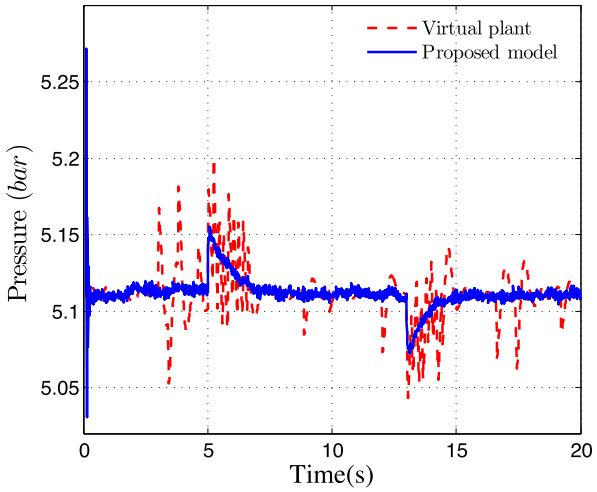

FIGURE 6. Air pressure of SOVCAAS on a quarter vehicle in co-simulation.

where we can see that the maximum error of air pressure is smaller than the value (0.25 bar) given in [17]. It is important to point out that the dynamic characteristics of AAS can be described by the proposed model, which is therefore accurate and better than the existing model in [17].

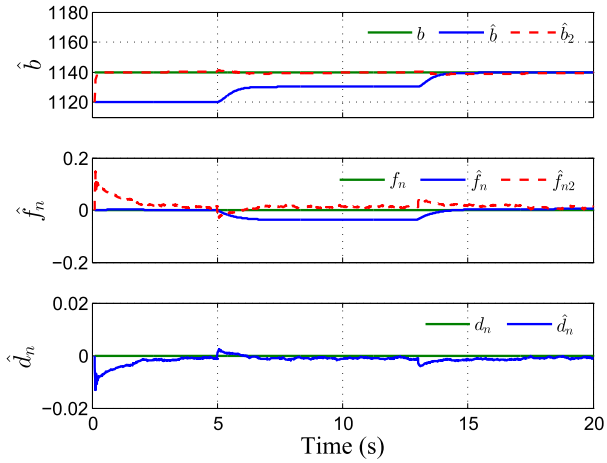

FIGURE 7. Parameter estimation of SOVCAAS on a quarter vehicle in co-simulation.

As displayed in Figure 7, the estimated parameters all converge and are close to their corresponding preset values through the parameter estimators. It means that the parameter estimators developed are effective and accurate. Moreover, the stability and robustness of the RHC system are guaranteed by the proposed controller, in which the designed parameter estimators dominate the *parametric uncertainties* in the proposed model.

Figure 8 displays the time evolution of e_1, e_2 and e_3. It can be seen that all of them converge on a neighborhood of zero as time increases during the period of each operation mode. Furthermore, when the virtual control input q_{LD} is synthesized by the proposed adaptive robust control law according to Equation (49), the desired air mass change $\dot{m}_{des}$ is

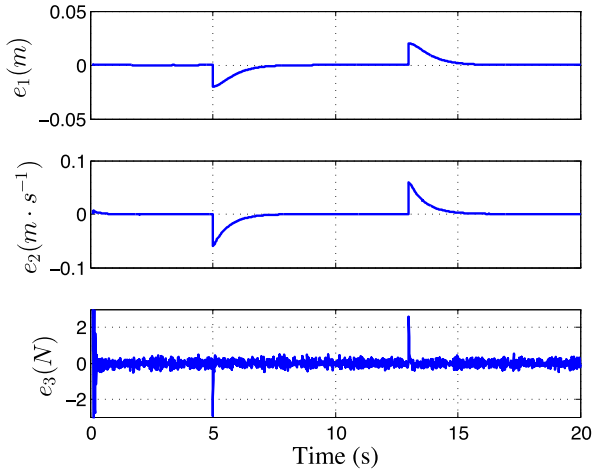

FIGURE 8. Tracking errors of SOVCAAS on a quarter vehicle in co-simulation.

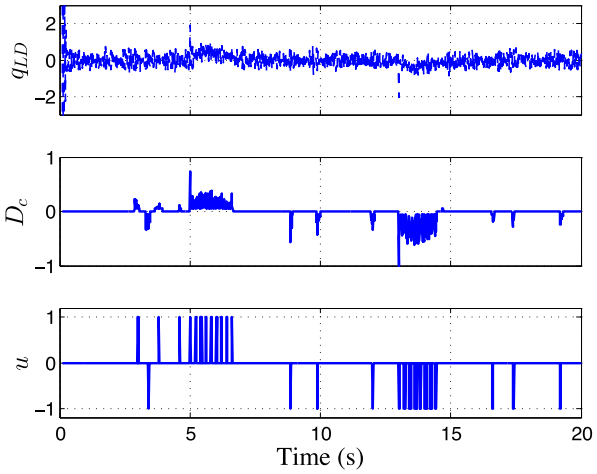

FIGURE 9. Control commands of SOVCAAS on a quarter vehicle in co-simulation.

calculated according to Equation (59) in Section VI-A, and then the control signal u can be converted into the corresponding PWM duty cycle for air inflating and deflating as shown in Figure 9. Under the same simulation parameters and road disturbance, Figure 4 also shows the simulation result of ride height with the PID controller and HMPC. The PID gains are determined by the Ziegler-Nichols method and the gains are $Kp = 0.3$, $Ki = 0.01$ and $Kd = 0.005$. Figure 4 shows the PID controller cannot track the desired height effectively due to the substantial overshooting and steady-state error during the control process. Therefore, the PID controller is not suitable for practical RHC with AAS system.

Compared with the latest and comparable technique HMPC [4], the *parametric uncertainties* are estimated through the use of a group of smooth projectors in the proposed control approach, while these are not fully considered in the HMPC. As a result, the proposed controller can achieve a better performance than the HMPC. The comparison of the performance indexes of HMPC, PID controller and proposed

TABLE 3. Performance index comparison of simulation results.

Performance index	HMPC		PID		Proposed Controller		Improvement (relative to HMPC)	
	Lev. up	Low. down	Lev. up	Low. down	Lev. up	Low. down	Lev. up	Low. down
RMS of ride height (mm)	8.5056	10.9886	8.8397	10.3764	5.5106	9.7765	35.21 %	11.03 %
SD of ride height (mm)	6.3912	7.9079	4.9074	6.5784	4.8326	7.1433	24.39 %	9.67 %
Adjustment time (s)	3.5	3.8	–	–	1.8	2	48.57 %	47.37 %

TABLE 4. Height error statistics of air spring model in steady state for RHC.

Height Error	RMS	SD
With considerations	2.2×10^{-4} m	2.1×10^{-4} m
Without considerations	1.9×10^{-3} m	1.7×10^{-3} m

controllers is shown in Table 3, which shows that the root mean square (RMS) and standard deviation (SD) of the ride height and adjustment time are decreased by using the proposed controller. The simulation results in Figure 4 and the performance comparison in Table 3 indicate that the proposed control technique is superior to the HMPC and PID controller.

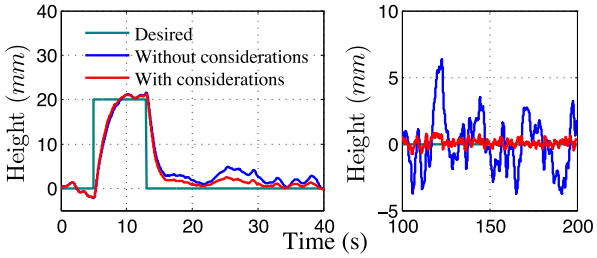

FIGURE 10. Height comparison of SOVCAAS with and without considerations of the parametric uncertainties and unmodeled dynamics on a quarter vehicle in co-simulation.

C. COMPARISON OF SIMULATION RESULTS

In order to further illustrate the benefits of the considerations of the *parametric uncertainties* and *unmodeled dynamics* in the proposed controller, Figure 10 displays the ride height of the air spring with/without the considerations of the *parametric uncertainties* and *unmodeled dynamics* in a simulation period of 200s. During the time form 100s to 200s, where the system stays in a steady state, as shown on the right side of Figure 11, the height error e_1 without the considerations of the *parametric uncertainties* and *unmodeled dynamics* is ultimately bounded by 6mm, which is much larger than the average 0.2 mm when using the proposed controller without the considerations of the *parametric uncertainties* and *unmodeled dynamics* as shown in Figure 11. The comparison of height error of the air spring model in steady state is described in Table 4.

VI. EXPERIMENTAL PLATFORM AND TEST

A. EXPERIMENTAL SETUP

To implement such a ride height system, a DC 12-V air compressor is employed to compress the air and then deliver the air to a tank. When the real air pressure reaches the

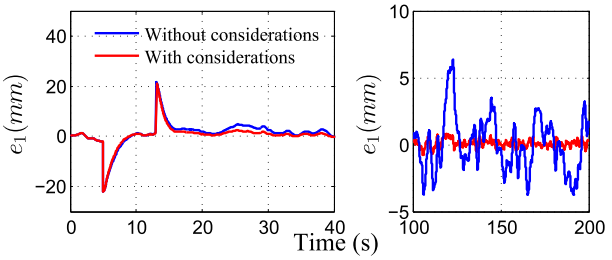

FIGURE 11. Height error comparison of SOVCAAS with and without considerations of the parametric uncertainties and unmodeled dynamics on a quarter vehicle in co-simulation.

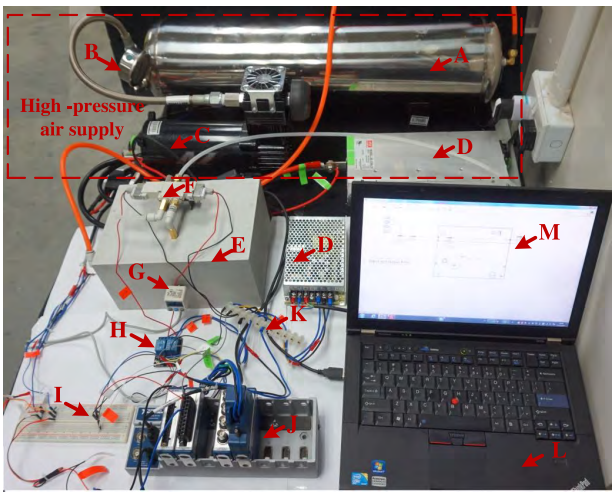

A. Air tank; B. Air pressure sensor; C. Air compressor; D. Direct current power supply source; E. Air box; F. 3-port 3-way solenoid actuated directional control valve; G. Pressure sensor; H. Electromagnetic relay; I. Terminal board; J. cRIO-9073 hardware; K. Extension wire board; L. Laptop computer; M. Control algorithm program built in LabView.

FIGURE 12. Experimental setup for air inflating and deflating system.

preset value, the air pressure sensor on the tank sends a signal to the relay, and then the air compressor power is cut off. When the air pressure inside the tank is lower than the preset air pressure value, the tank-air pressure sensor generates a control signal to activate the air compressor. The detailed experimental setup for air inflating and deflating is shown in Figure 12. In order to ensure a steady delivery of the high-pressure air mass, an air box is fabricated to store the high-pressure air temporarily. Additionally, the RHC system consists of a laptop computer (CPU i7-4770 3.40 GHz), a National Instruments cRIO-9073 (8-Slot, 266 MHz CPU, 64 MB DRAM, 128 MB Storage) embedded controller [33],

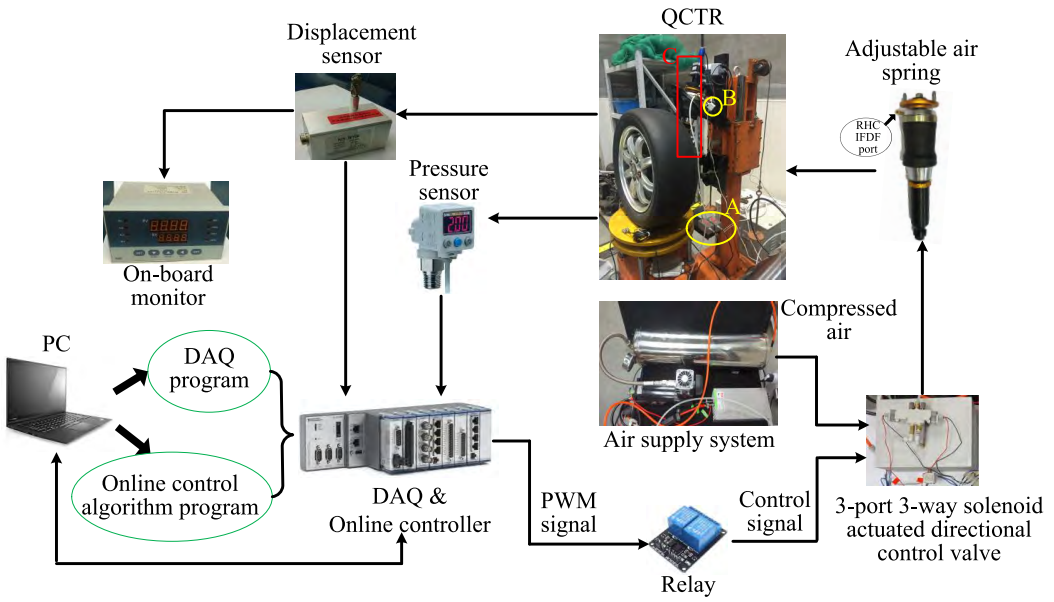

FIGURE 13. Experimental setup of SOVCAAS on the quarter car test rig.

three ride height sensors, two solid-state relays, a 3-port 3-way directional control valve and an air pressure sensor.

The experimental setup of the RHC system is designed by combining an in-house quarter car test rig (QCTR) with the SOVCAAS. The implementation and testing of the RHC system can be achieved on the QCTR as shown in Figure 13. During the RHC process, an air pressure sensor is used to measure the pressure inside the air spring, and two displacement sensors are employed to monitor the height changes of the sprung mass and the unsprung mass, respectively. By using the Measurement and Automation Explorer (MAX) software installed in a laptop computer, we can create and edit channels, tasks, and interface with the SOVCAAS system. The data acquisition (DAQ) procedure is compiled into a virtual instrument (VI) program to measure the electrical or physical signals, such as voltage and current from sensors in LabView software. The proposed control algorithm programmed in MatLab/Simulink is able to run the script module in the VI program. The C code of the VI program can also be generated automatically. It is then stored in the NI cRIO-9073 hardware so that the air pressure and height information can be obtained in a real-time manner.

In order to illustrate the operation details of leveling up and lowering down procedures, a schematic of the active air spring system for a quarter car is provided in Figure 14. The leveling up and lowering down procedures of the target air suspension are as follows,

1) *Leveling up procedure*: The solid line in Figure 14 shows how to increase air mass in the air spring for leveling up the sprung mass. When the air pressure in the air tank is smaller than 8 bar, the compressor starts to work and provides the high-pressure air in the air tank. The compressed air flows from the air tank to the air spring through the air box and the directional control valve, which regulates air flow into the corresponding air spring in an on-off manner.
2) *Lowering down procedure*: When the vehicle height needs to be lowered, the control signal from the electronic control unit switches the directional control valve spool to the opposite position. Then, the air in the air spring deflates to the atmosphere, thus the volume of the air spring decreases and then the vehicle height drops.

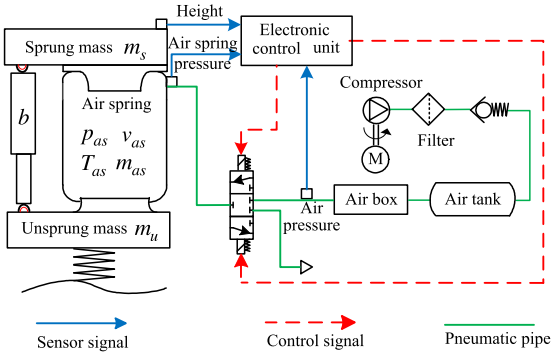

FIGURE 14. Circuit diagram of RHC for a quarter vehicle air suspension.

Therefore, the control operation can be one of the following three procedures,

Pro.I *Leveling up*: according to Equation (1), the maximum increment of the air mass within a PWM period T_p an be expressed as,

$$\begin{cases} \dot{m}_{in} = q(p_s, p_{as})T_p, \\ \dot{m}_{out} = 0. \end{cases} \tag{56}$$

where p_s is the upstream pressure and p_{as} is the downstream pressure in the leveling process;

Pro.II *Lowering down*: according to Equation (1), the maximum decrement of the air mass within a PWM period T_p can be expressed as,

$$\begin{cases} \dot{m}_{in} = 0, \\ \dot{m}_{out} = q(p_{as}, p_e)T_p. \end{cases} \tag{57}$$

where p_{as} is the upstream pressure and p_e is the downstream pressure in the lowering process;

Pro.III *Hold*: both of the valves are closed, the air mass in the spring remains unchanged as,

$$\dot{m}_{in} = \dot{m}_{out} = 0. \tag{58}$$

Thereby, once the virtual control input q_{LD} is chosen, the desired air mass change $\dot{m}_{des}$ is calculated according to Equation (18) as,

$$\dot{m}_{des} = \begin{cases} s_p v_{as} q_{LD}/(\gamma R T_s) & \text{if } q_{LD} > 0, \\ s_p v_{as} q_{LD}/(-\gamma R T_{as}) & \text{if } q_{LD} \le 0. \end{cases} \tag{59}$$

The corresponding PWM duty cycle (D_c) of the chosen virtual control input q_{LD} can be viewed as the control signal which can be determined as,

$$\begin{cases} Pro.I : D_c = \min\left(\dfrac{q_{LD} s_p v_{as}}{\dot{m}_{in} \gamma R T_s}, 1\right), \\ Pro.II : D_c = \min\left(\dfrac{q_{LD} s_p v_{as}}{-\dot{m}_{out} \gamma R T_s}, 1\right), \\ Pro.III : D_c = 0. \end{cases} \tag{60}$$

When there is a demand for ride height adjustment, the cRIO-9073 generates the control signal with the corresponding PWM duty cycle according to Equation (60). The solenoid-operated electro-pneumatic valve receives this control signal to provide a fully open or fully closed position for the valve port so that the air inflating and deflating (IFDF) port can be opened until reaching the target height that is measured by the ride height sensor. The prototype and regulating mechanism of the adjustable air spring are shown in Figure 13.

B. TEST RESULTS

The proposed controller is tested for tracking a height profile of easy entry mode, and the experimental results are presented in this section. The parameters of the SOVCAAS used in the experimental tests are given by: $m_s = 90\,\text{kg}$, $m_u = 20\,\text{kg}$, $p_0 = 2.5\,\text{bar}$, $k_1 = 1$, $k_2 = 450$, $k_3 = 50$, $\lambda_1 = 1.7 \times 10^4$, $\lambda_2 = 5$, $\lambda_3 = 43$, $\lambda_4 = -0.08$, and $\lambda_5 = 0.5 \times 10^{-3}$.

Figure 15 shows the time evolution of the desired and actual heights of the proposed controller in both simulation result (Pro. Con. in Sim.) and experimental result (Pro. Con. in Exp.), PID controller with the same gains as in the simulation and the HMPC [4]. Figure 15 presents the proposed controller can track closely to the desired ride height within 2.5 s during both leveling up (time from 0 s to t_{e1}) and lowering down (time from 10 s to t_{e2}) processes, and the height

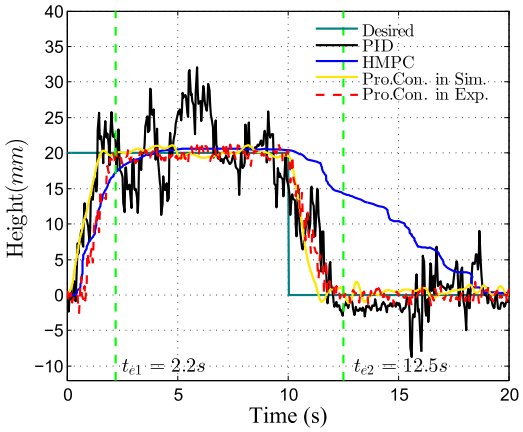

FIGURE 15. Height tracking of SOVCAAS on the quarter car test rig.

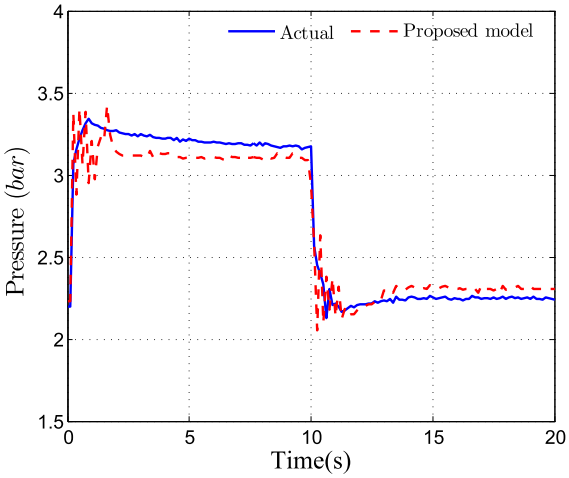

FIGURE 16. Pressure of SOVCAAS on the quarter car test rig.

tracking error is within the tolerance of ± 1 mm, while the PID controller cannot track the desired height and the HMPC takes a longer time. Moreover, the experimental result of the proposed controller is in good agreement with its simulation result except for a time delay caused by the signal processing and hardware action. It is noteworthy that the result of HMPC in Figure 15 is captured from [4]. However, due to the existence of sensor noises during the experimental test, there always exist ripples in Figure 15. Because of considering the *unmodeled dynamics* and *parametric uncertainties* in the AAS, the pressure value of the air spring described in the mathematical model can approximate to the actual one as displayed in Figure 16.

During both leveling up and lowering down processes, the stability and robustness of the proposed controller with the designed parameter estimators are validated with the experimental results in Figures 17 and 18. As shown in Figure 17, the estimates of *parametric uncertainties* converge and are close to their corresponding desired values. Moreover, Figure 18 depicts that the time evolution of the errors e_1, e_2 and e_3 can converge on a neighborhood of zero,

TABLE 5. Performance index comparison of experimental tests.

Performance index	HMPC		PID		Proposed Controller		Improvement (relative to HMPC)	
	Lev. up	Low. down	Lev. up	Low. down	Lev. up	Low. down	Lev. up	Low. down
RMS of ride height (mm)	10.5489	11.5936	6.7025	5.0843	6.8944	4.7178	34.64 %	59.31 %
SD of ride height (mm)	6.7301	6.1089	4.5769	3.7380	6.1184	4.2211	9.09 %	30.9 %
Adjustment time (s)	4	10	–	–	2.2	2.5	45 %	75 %

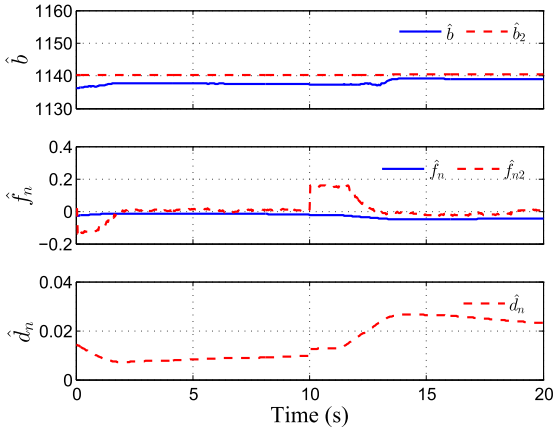

FIGURE 17. Parameter estimation of SOVCAAS on the quarter car test rig.

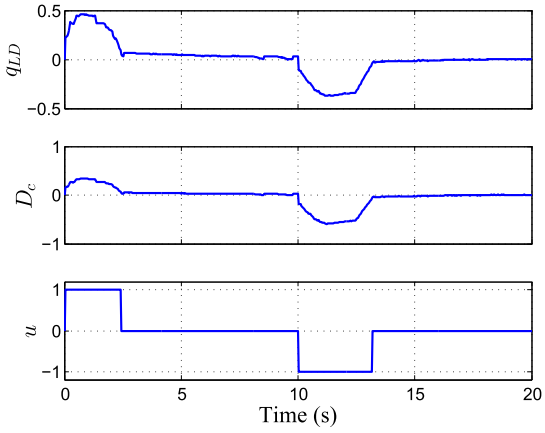

FIGURE 19. Actuator commands of SOVCAAS on the quarter car test rig.

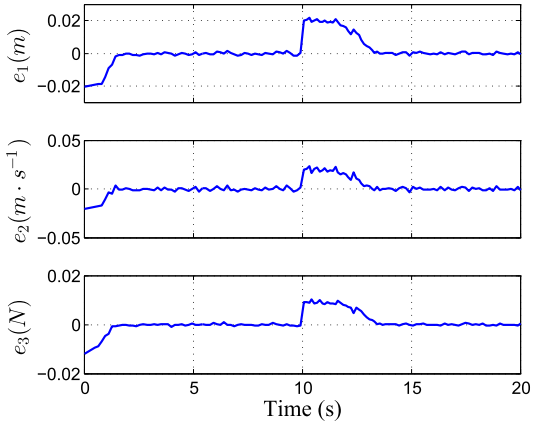

FIGURE 18. Tracking error of SOVCAAS on the quarter car test rig.

achieving GUUB. Figure 19 shows the virtual control input q_{LD} and the corresponding duty cycle of PWM as the control signal u for air inflating and deflating. Furthermore, it is noted that the convergence rate of the experimental results is slower as compared with the simulation results presented in Section V-A due to the existence of signal disturbance, and the time delays caused by the sensors and the executive component of pneumatic system in the experiment.

The performance index comparison of the experimental results is described in Table 5. Compared with the HMPC, the RMS and SD of the ride height are reduced by the PID controller. However, the PID controller is unable to track the desired height value and even unstable so that there is no adjustment time. Compared with the HMPC, the RMS and SD of ride height are decreased by the proposed controller with a faster adjustment time than that in the HMPC. Figure 15 and Table 5 display that the proposed controller outperforms the latest technique [4] and PID controller for RHC.

Overall, the experimental results show that the proposed control technique is also effective in practice. Experimental video is presented in [34].

VII. CONCLUSION

This paper presents a new solution to the task of height tracking for an electronically-controlled AAS system. A mathematical model of AAS is first formulated into a nonlinear system form, in which *parametric uncertainties* and *unmodeled dynamics* are fully considered for model-based controller design. Then, an adaptive robust controller is proposed by employing the technique of backstepping which can drive the ride height to the neighborhood of the desired values during each operation mode. By using a projection operator, parameter estimators are designed to ensure the *parametric uncertainties* remain within predefined corresponding bounds. Moreover, some conservativeness is introduced in this control law to dominate the *unmodeled dynamics* while guaranteeing robustness under the uncertain time-varying disturbances. Simulation and experimental results illustrate that the proposed control method is effective, robust, and superior to the recent technique.

With respect to future work, an adaptive robust synchronized control system will be designed to adjust the full vehicle body by controlling the heights of four electronically-controlled air springs simultaneously for improvement of ride comfort, road holding capacity and handling stability.

REFERENCES

[1] J. Zhao P. K. Wong, X. Ma, and Z. Xie, "Chassis integrated control for active suspension, active front steering and direct yaw moment systems using hierarchical strategy," *Veh. Syst. Dyn.*, vol. 55, no. 1, pp. 72–103, Jan. 2017.
[2] J. Zhao, P. K. Wong, Z. Xie, C. Wei, and F. He, "Integrated variable speed-fuzzy PWM control for ride height adjustment of active air suspension systems," in *Proc. Amer. Control Conf.*, Chicago, IL, USA, Jul. 2015, pp. 5700–5705.
[3] A. A. Aly and F. A. Salem, "Vehicle suspension systems control: A review," *Int. J. Control Autom. Syst.*, vol. 2, no. 2, pp. 46–54, Jul. 2013.
[4] X. Sun, Y. Cai, L. Chen, Y. Liu, and S. Wang, "Vehicle height and posture control of the electronic air suspension system using the hybrid system approach," *Veh. Syst. Dyn.*, vol. 54, no. 3, pp. 328–352, Jan. 2016.
[5] F. Löcken and M. Welsch, "The dynamic characteristic and hysteresis effect of an air spring," *Int. J. Appl. Mech. Eng.*, vol. 20, no. 1, pp. 127–145, 2015.
[6] A. J. Nieto, A. L. Morales, A. González, J. M. Chicharro, and P. Pintado, "An analytical model of pneumatic suspensions based on an experimental characterization," *J. Sound Vib.*, vol. 313, nos. 1–2, pp. 290–307, Jun. 2008.
[7] S. J. Lee, "Development and analysis of an air spring model," *Int. J. Automot. Technol.*, vol. 11, no. 4, pp. 471–479, Aug. 2010.
[8] H. Liu and J. C. Lee, "Model development and experimental research on an air spring with auxiliary reservoir," *Int. J. Automot. Technol.*, vol. 12, no. 6, pp. 839–847, Dec. 2011.
[9] P. K. Wong, Z. Xie, J. Zhao, T. Xu, and F. He, "Analysis of automotive rolling lobe air spring under alternative factors with finite element model," *J. Mech. Sci. Technol.*, vol. 28, no. 12, pp. 5069–5081, Dec. 2014.
[10] F. Chang and Z.-H. Lu, "Dynamic model of an air spring and integration into a vehicle dynamics model," in *Proc. Inst. Mech. Eng. D, J. Automobile Eng.*, vol. 222, no. 10, pp. 1813–1825, Oct. 2008.
[11] B. Yao and M. Tomizuka, "Adaptive robust control of MIMO nonlinear systems in semi-strict feedback forms," *Automatica*, vol. 37, no. 9, pp. 1305–1321, Sep. 2001.
[12] H. K. Lee, G. S. Choi, and G. H. Choi, "A study on tracking position control of pneumatic actuators," *Mechatronics*, vol. 12, no. 6, pp. 813–831, Jul. 2002.
[13] Z. Situm, D. Pavkovic, and B. Novakovic, "Servo pneumatic position control using fuzzy PID gain scheduling," *J. Dyn. Syst. Meas. Control*, vol. 126, no. 2, pp. 376–387, Jun. 2004.
[14] Y.-C. Tsai and A.-C. Huang, "Multiple-surface sliding controller design for pneumatic servo systems," *Mechatronics*, vol. 18, no. 9, pp. 506–512, Nov. 2008.
[15] R. Richardson, A. R. Plummer, and M. D. Brown, "Self-tuning control of a low-friction pneumatic actuator under the influence of gravity," *IEEE Trans. Control Syst. Technol.*, vol. 9, no. 2, pp. 330–334, Mar. 2001.
[16] F. Zhao, S. S. Ge, F. Tu, Y. Qin, and M. Dong, "Adaptive neural network control for active suspension system with actuator saturation," *IET Control Theory Appl.*, vol. 10, no. 14, pp. 1696–1705, Sep. 2016.
[17] H. Kim and H. Lee, "Height and leveling control of automotive air suspension system using sliding mode approach," *IEEE Trans. Veh. Technol.*, vol. 60, no. 5, pp. 2027–2041, Jun. 2011.
[18] A. Girin, F. Plestan, X. Brun, and A. Glumineau, "High-order sliding-mode controllers of an electropneumatic actuator: Application to an aeronautic benchmark," *IEEE Trans. Control Syst. Technol.*, vol. 17, no. 3, pp. 633–645, May 2009.
[19] X.-Q. Sun, Y.-F. Cai, C.-C. Yuan, S.-H. Wang, and L. Chen, "Fuzzy sliding mode control for the vehicle height and leveling adjustment system of an electronic air suspension," *Chin. J. Mech. Eng.*, vol. 31, no. 1, p. 25, Dec. 2018.
[20] M. Smaoui, X. Brun, and D. Thomasset, "A study on tracking position control of an electropneumatic system using backstepping design," *Control Eng. Pract.*, vol. 14, no. 8, pp. 923–933, Aug. 2006.
[21] Z. Rao and G. M. Bone, "Nonlinear modeling and control of servo pneumatic actuators," *IEEE Trans. Control Syst. Technol.*, vol. 16, no. 3, pp. 562–569, May 2008.
[22] M.-M. Ma and H. Chen, "Disturbance attenuation control of active suspension with non-linear actuator dynamics," *IET Control Theory Appl.*, vol. 5, no. 1, pp. 112–122, Jan. 2011.
[23] C. Chen, C. Wen, Z. Liu, K. Xie, Y. Zhang, and C. L. P. Chen, "Adaptive asymptotic control of multivariable systems based on a one-parameter estimation approach," *Automatica*, vol. 83, pp. 124–132, Sep. 2017.
[24] C. Wang and Y. Lin, "Multivariable adaptive backstepping control: A norm estimation approach," *IEEE Trans. Autom. Control*, vol. 57, no. 4, pp. 989–995, Apr. 2012.
[25] Q. Wang and R. F. Stengel, "Robust control of nonlinear systems with parametric uncertainty," *Automatica*, vol. 38, no. 9, pp. 1591–1599, Sep. 2002.
[26] D. Y. Meng, G. Tao, A. Li, and W. Li, "Precision synchronization motion trajectory tracking control of multiple pneumatic cylinders," *Asian J. Control*, vol. 18, no. 5, pp. 1749–1764, Sep. 2016.
[27] X. R. Shen, J. Zhang, E. J. Barth, and M. Goldfarb, "Nonlinear model-based control of pulse width modulated pneumatic servo systems," *J. Dyn. Syst., Meas., Control*, vol. 128, no. 3, pp. 663–669, Sep. 2006.
[28] J. F. Carneiro and F. G. de Almeida, "Reduced-order thermodynamic models for servo-pneumatic actuator chambers," *Proc. Inst. Mech. Eng. I, J. Syst. Control Eng.*, vol. 220, no. 4, pp. 301–314, Jun. 2006.
[29] M. M. Polycarpou, "Stable adaptive neural control scheme for nonlinear systems," *IEEE Trans. Autom. Control*, vol. 41, no. 3, pp. 447–451, Mar. 1996.
[30] Z. Cai, M. S. de Queiroz, and D. M. Dawson, "A sufficiently smooth projection operator," *IEEE Trans. Autom. Control*, vol. 51, no. 1, pp. 135–139, Jan. 2006.
[31] W. Xie, D. Cabecinhas, R. Cunha, and C. Silvestre, "Robust motion control of an underactuated hovercraft," *IEEE Trans. Control Syst. Technol.*, to be published.
[32] (Jan. 2019). *International Organization for Standardization*. [Online]. Available: https://www.iso.org/standard/71202.html
[33] (Jan. 2019). *National Instrument*. [Online]. Available: http://www.ni.com/en-us/support/model.crio-9073.html
[34] (Jan. 2019). *Experimental Test Video*. [Online]. Available: http://www.fst.umac.mo/en/lab/ael/Road%20Disturbance%20for%20papre%20RHC.mp4

RONGCHEN ZHAO received the M.Sc. degree from the School of Mechanical Engineering, Guizhou University, in 2014. He is currently pursuing the Ph.D. degree with the Department of Electromechanical Engineering, University of Macau.

His research interests include automotive engineering, chassis control, adaptive cruise control, and cooperative control of multiple vehicles.

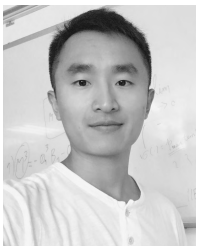

WEI XIE received the M.Sc. degree in electromechanical engineering from the University of Macau, in 2016, where he is currently pursuing the Ph.D. degree with the Sensor-Based Cooperative Robotics Laboratory, Faculty of Science and Technology.

From 2017 to 2018, he was a Visiting Scholar with the Instituto Superior Técnico, Universidade de Lisboa, Lisbon, Portugal. His current research interests include nonlinear control, motion control of ocean and air vehicles, and coordinated control of multiple agents.

PAK KIN WONG received the Ph.D. degree in mechanical engineering from The Hong Kong Polytechnic University, Hong Kong, in 1997.

He is currently a Professor with the Department of Electromechanical Engineering and an Associate Dean (Academic Affairs) of the Faculty of Science and Technology, University of Macau. He has published over 200 scientific papers in refereed journals, book chapters, and conference proceedings. His research interests include automotive engineering, fluid transmission and control, artificial intelligence, mechanical vibration, and medical engineering.

DAVID CABECINHAS received the Licenciatura and Ph.D. degrees in electrical and computer engineering from the Instituto Superior Técnico (IST), Lisbon, Portugal, in 2006 and 2014, respectively.

Since 2007, he has been a Researcher with the Laboratory for Robotics and Engineering Systems, Institute for Systems and Robotics, Lisbon. He is currently a Postdoctoral Fellow with the Faulty of Science and Technology, University of Macau, Macau, China. His current research interests include nonlinear control, sensor-based and vision-based control with applications to autonomous aerial and surface vehicles, and modeling and identification of aerial and surface vehicles.

CARLOS SILVESTRE received the Licenciatura and master's degrees in electrical engineering, the Ph.D. degree in control science, and the Habilitation degree in electrical engineering and computers from the Instituto Superior Técnico (IST), Lisbon, Portugal, in 1987, 1991, 2000, and 2011, respectively.

Since 2000, he has been with the Department of Electrical Engineering, IST. He is currently on leave. Since 2015, he has been a Professor with the Department of Electrical and Computer Engineering, Faculty of Science and Technology, University of Macau, Macau, China. His current research interests include linear and nonlinear control theory, hybrid systems, multi-agent control systems, networked control systems, inertial navigation systems, and real-time architectures for complex autonomous systems with applications to unmanned air and underwater vehicles.